MR_Go: A Magnetorheological Quadruped Robot for Energy-Efficient, High-Payload, and Impact-Tolerant Planetary Exploration

Erwin Ang Tien Yew, Zhehan Tao, Haorui Cai, Zhongyuan Kong, Bingbing Zhou, Liang Zhang, and Shuaishuai Sun

***Abstract*—Planetary exploration missions increasingly rely on agile robotic platforms capable of traversing unstructured and unpredictable terrain. While quadruped robots offer superior mobility compared to wheeled rovers, their deployment in long-duration and shock-load missions remains limited, due to the limitations of high power consumption, low payload-to-weight ratio, and poor resilience to impact and overloads with the conventional actuator. To address these challenges, we present the MR_Go, a magnetorheological (MR)-based quadruped robot featuring real-time joint damping modulation to enhance energy efficiency, impact mitigation, and load-bearing capability. Built upon the Unitree Go1 platform, MR_Go achieves a 400% increase in payload-to-mass ratio with only 40 W of MR activation power and can sustain 20 kg payloads without continuous motor engagement. Experiments conducted in lunar-analog terrain demonstrate that MR_Go extends mission battery life by 18%, reduces peak joint torque by 10% during an 80 cm cliff drop, and maintains superior thermal stability under prolonged loading. These results highlight the potential of MR-based hybrid actuation for enabling durable and energy-efficient quadruped systems suited for extended planetary operations.**

***Index Terms*—Actuation and joint mechanisms, field robots, legged robots.**

Received 13 November 2025; accepted 10 March 2026. Date of publication 19 March 2026; date of current version 26 March 2026. This article was recommended for publication by Associate Editor R. Qi and Editor C. D. Santina upon evaluation of the reviewers' comments. This work was supported in part by the National Natural Science Foundation of China under Grant U21A20119, Grant 52105081, and Grant 62303002, in part by the Major Project of Anhui Province's Science and Technology Innovation Breakthrough Plan under Grant 202423h08050003, in part by the State Key Laboratory of Micro-Spacecraft Rapid Design and Intelligent Cluster under Grant MS01240110, in part by the Major Project of Anhui Province's Science and Technology Innovation Breakthrough Plan under Grant 202423h08050003, in part by the Anhui's Key R&D Program of China under Grant 202104a05020009, in part by USTC Start-Up Funding under Grant KY2090000067, and in part by the Fundamental Research Funds for the Central Universities under Grant SC5290005162. *(Corresponding authors: Liang Zhang; Shuaishuai Sun.)*

Erwin Ang Tien Yew, Zhehan Tao, Haorui Cai, Zhongyuan Kong, Bingbing Zhou, and Shuaishuai Sun are with the CAS Key Laboratory of Mechanical Behavior and Design of Materials, School of Engineering Sciences, Institute of Humanoid Robots, University of Science and Technology of China, Hefei 230026, China (e-mail: etya1a17@mail.ustc.edu.cn; tzh992171976@mail.ustc.edu.cn; harry31@mail.ustc.edu.cn; zhongyuan_kong@mail.ustc.edu.cn; zhoubingbing@mail.ustc.edu.cn; sssun@ustc.edu.cn).

Liang Zhang is with the School of Electrical Engineering and Automation, Anhui University, Hefei 230601, China (e-mail: liangzhang@ahu.edu.cn).

This article has supplementary downloadable material available at https://doi.org/10.1109/LRA.2026.3675964, provided by the authors.

Digital Object Identifier 10.1109/LRA.2026.3675964

I. Introduction

Quadrupedal robots have emerged as a viable alternative for the large-scale exploration of unstructured terrain on planetary surfaces [1], [2]. However, current fully electric-driven quadrupedal robots are limited by high power consumption [3], a low payload-to-weight ratio [4], and poor resilience to impacts and overloads [5], which in turn limits their widespread application in planetary exploration, such as sustaining a heavy scientific payload in a standing posture over extended durations, conducting high-altitude leaps with a high-impact landing for crater or water-ice detection, and so on.

Recent research has sought to address these challenges through advancements in actuation technologies. The introduction of Series Elastic Actuator (SEA) [6], implemented in quadruped robots such as ANYmal [7] and StarlETH [8], improves compliance [9] and facilitated impact absorption; however, SEAs require continuous motor engagement to maintain precise trajectory control, offering limited relief from actuator workload and energy consumption. Parallel Elastic Actuators (PEAs) [10] have been further explored to enhance torque density and energy efficiency, with systems such as AoPS [11] and Tachyon [12] reporting notable reductions in energy and power consumption during cyclic locomotion and static postures. To address the frequency-dependent limitations of fixed-stiffness PEAs, Variable Stiffness Actuators (VSAs) have been proposed to adapt joint stiffness and enable resonance tracking over a range of oscillation frequencies, thereby improving efficiency in cyclic motions with varying gait speed or cadence [13]. Nonetheless, prior studies [10] have shown that stiffness loses effectiveness during non-cyclic tasks or when operating on unpredictable terrain, limiting their applicability to planetary or field environments.

Magnetorheological fluids (MRF)s [17] have recently emerged as a promising smart material due to their ability to rapidly alter viscosity and rheological properties in response to an applied magnetic field. This field-dependent tunability enables MRF-based systems to efficiently dissipate energy and absorb impact forces by increasing their apparent viscosity during dynamic events. MR devices such as MR dampers, brakes, and clutches have been extensively applied in exoskeletons [18], [19] and robotic manipulators [20], [21], demonstrating their effectiveness in achieving controllable compliance and adaptive damping in compact robotic systems.

Specifically, [22] presented a non-motorized hand exoskeleton based on Magnetorheological Actuator (MRA) that achieved

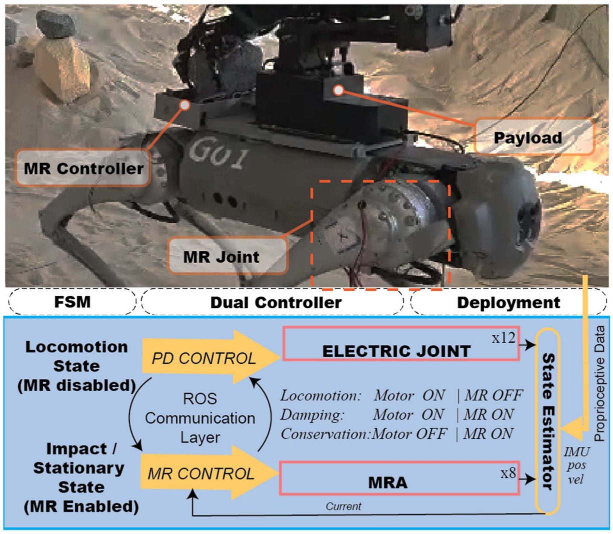

Fig. 1. Overview of MR-based Go Quadruped Robot (MR_Go), the proposed MR-based quadruped robot. Eight thigh and calf joints are each equipped with an Magnetorheological Actuator (MRA) providing field-controllable damping and locking. The figure illustrates the dual-layer control architecture, where MR actuation is selectively enabled based on robot state estimation while electric motors govern nominal joint motion.

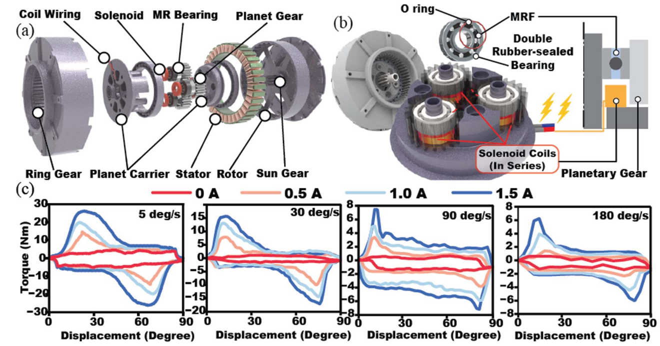

Fig. 2. Magnetorheological actuator (MRA): (a) Exploded view. (b) Separation and section view of MR planetary module from the electric actuator. (c) Torque–displacement responses under different angular speeds (5 °/s to 180 °/s) and excitation currents (0 to 1.5 A).

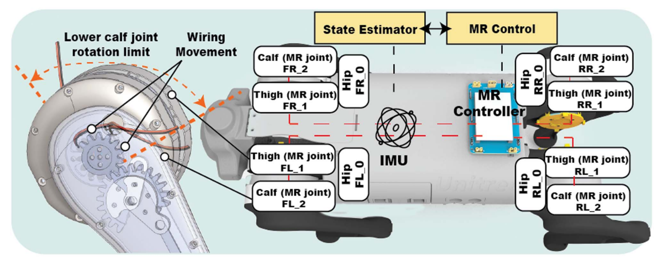

Fig. 3. System architecture of MR_Go, illustrating the integration of MR joint actuation.

a peak holding force of 1046 N with only 5 W of input power, demonstrating the high force-to-power ratio achievable through MR actuation. [23] introduced a lower-limb exoskeleton incorporating a variable-displacement, permanent-magnet MR damper at the knee joint to assist load transfer, which effectively mitigated impact by reducing ground-reaction-force peaks by 24% (early stance) and 19% (late stance). Similarly, [24] developed a magnetorheologically damped compliant foot for the HyQ quadruped, combining a linear spring with an MR damper. The prototype achieved a controllable force range of 15-485 N, and drop tests from 0.1-0.3 m demonstrated up to 98% reduction in bounce, validating the effectiveness of MR-based damping in mitigating impact energy and improving ground-contact stability during locomotion. While Variable Stiffness Actuators regulate mechanical impedance by modulating conservative energy storage, MR-based actuators fundamentally differ by directly controlling energy dissipation through field-dependent damping. This distinction enables MRA to remain effective during non-periodic, impact-dominated interactions and prolonged static load-bearing, where stiffness adaptation alone provides limited authority and continued motor intervention is often required.

Our goal is to enhance the performance of conventional electrically actuated quadruped robots while preserving their inherent advantages in control precision and efficiency. The main conceptual challenge lies in integrating an additional MR-based actuation layer alongside the existing electric actuation system within a compact quadruped platform. Achieving this requires co-designing both the mechanical and control architectures to enable real-time coordination between MR damping and electric torque control while maintaining overall system stability and compactness. Specifically, this work addresses three key challenges: (1) designing MR hardware that introduces minimal increases in system weight and volume; (2) developing a unified low-level control framework that enables seamless coordination between MR damping and active electric actuation; and (3) ensuring system stability and reliability across diverse operational scenarios, including impact events, payload handling, and prolonged exploration tasks.

This letter introduces MR_Go (Fig. 1), a compact MR-based quadruped robot that is optimized by replacing eight calf and thigh joints with the light-weight MRA [25] on the commercial Unitree Go1 platform. The contributions of this work are summarized as follows:

1) **Compact MR hardware design:** Development and integration of a lightweight MRA and a four-channel current-control module delivering high lockup torque, rapid energy dissipation, and low power consumption with minimal increases in system weight and volume.
2) **Unified hybrid control framework:** Formulation of a Finite State Machine (FSM) architecture that coordinates low-level MR damping and electric actuation, enabling efficient impact mitigation and energy-saving behaviors during high-load or dynamic planetary exploration tasks.
3) **Experimental validation in lunar-analog terrain:** Demonstration of improved energy efficiency, enhanced impact resilience, and extended operational endurance compared with a baseline quadruped, confirming the feasibility of MR-based hybrid actuation for long-duration exploration missions.

II. System Description

A. Mechanical Design

As shown in Fig. 2 and Fig. 3, the MRA integrated into MR_Go retains the same external volume as the conventional electric actuator, with only a marginal mass increase of 60 g (approximately 10% of the original mass). Each MRA Fig. 2(a) replaces the conventional needle bearing with a precision deep-groove ball bearing (619/6.2RSR.P5 BKD), incorporates three solenoid coils (156 turns of 0.25 mm copper wire connected in series), and integrates a ferromagnetic planetary gear assembly. This placement allows the MR element within the planetary gearbox to operate at the lower rotational speeds of the geared stage, where yield-dominated MR damping is more pronounced, avoiding high-speed shear conditions associated with rotor-side integration.

Each MR bearing is filled with approximately 0.1 ml of MRF (87.7 wt%), enabling field-responsive damping behavior. The MR bearings are interference-fitted into the planet carrier and planet gear using Loctite 638 adhesive, ensuring precise alignment and a single rotational DOF for efficient torque transmission through the MR interface. Appropriate mechanical clearances are maintained to prevent interference between rotating components.

The custom solenoid design enables efficient magnetic flux generation within the compact planetary volume while avoiding conflicts with moving parts, as shown in the sectional view in Fig. 2(b). The MR planetary assembly integrates seamlessly into the actuator ring housing, with paired coil terminals providing current input for real-time damping control. Fig. 2(c) also illustrates the current-dependent response of the MRA under a 90° input amplitude for coil currents ranging from 0 to 1.5 A. Experiments were conducted at angular speeds of 5°/s, 30°/s, 90°/s, and 180°/s to evaluate performance across different operating conditions. The prototype achieved a maximum damping torque of 26.15 Nm at 1.5 A, corresponding to a torque-to-mass ratio of 52.3 Nm/kg and a torque-to-volume ratio of 14.6 Nm/mm^3. Comprehensive design specifications and characterization procedures are detailed in [25].

B. Analytical Model of Hybrid Torque Coordination

The MRA operates by exploiting the field-dependent rheology of the enclosed MR fluid, whereby an applied magnetic field induces rapid particle chain formation that increases effective shear resistance and generates a controllable resistive torque. To accurately represent this hybrid actuation behavior, the MR damping term was calibrated using experimental characterization data and validated through COMSOL simulations. An analytical torque model is then formulated to describe the coupling between electric and MR actuation, providing both a theoretical foundation and a quantitative interpretation of the observed system behavior [26], [27].

Based on [28], where the electric motor and MR brake share a common output shaft and operate in a torque-parallel configuration, the total joint torque can be expressed as the superposition of the motor-generated torque and the MR-induced resistive torque. Under this framework, the MR element acts as a semi-active impedance modulator that contributes an additive resistive torque without altering the motor control law.

Accordingly, during hybrid operation, the commanded joint torque τ_j is modeled as:

$$\tau_j(t) = \underbrace{K_p(\theta_{\text{cmd}} - \theta) + K_d\,\dot{\theta}}_{\text{Electric motor control}} + \underbrace{\tau_{\text{off}} + \tau_{\text{MR}}}_{\text{Passive and MR contribution}}. \quad (1)$$

Under this formulation, the electric motor generates the primary motion command, while the MR actuator modulates joint impedance through a semi-active resistive torque without modifying the motor control law. The passive term τ_{off} represents the off-state drag torque of the MR mechanism.

The MR-induced torque is described using a regime-based, control-oriented model:

$$\tau_{\text{MR}} = \begin{cases} \tau_y(I)\,\text{sgn}(\dot{\theta}), & |\tau_{\text{impact}}| < \tau_y(I) \quad \text{(pre-yield)}, \\ b(I)\,\dot{\theta}, & |\tau_{\text{impact}}| \geq \tau_y(I) \quad \text{(post-yield)}, \end{cases} \quad (2)$$

where $\tau_y(I)$ denotes the field-dependent yield torque and $b(I)$ is the current-dependent viscous damping coefficient.

During sudden contact events (e.g., impact or step loading), the MR response is initially governed by the pre-yield regime, in which the field-dependent yield torque $\tau_y(I)$ provides an immediate and bounded resistive torque that opposes rapid joint motion. If $|\tau_{\text{impact}}| < \tau_y(I)$, joint motion is effectively suppressed, yielding a high-impedance, near-zero-velocity response. When the applied load exceeds $\tau_y(I)$, the MRF yields and the response transitions smoothly into the post-yield regime, where the MR element behaves as a controllable viscous damper $b(I)\dot{\theta}$.

To ensure efficient cooperation between the joint motor and the MR element, the MR current is regulated by a state-gated supervisory scheduler. MR actuation is disabled during nominal locomotion ($I = 0$) to avoid injecting task-dependent impedance into the gait controller, and is enabled only in MR-enhanced FSM states (e.g., impact mitigation and stationary support). In MR-enabled states, the commanded current is computed from proprioceptive measurements and bounded by hardware limits:

$$I_{\text{cmd}} = \Gamma(s)\begin{cases} I_{\text{base}}, & |a_z| \leq a_{\text{th}} \quad \text{(quasi-static support)}, \\ I_{\text{low}}, & |\dot{\theta}| < \omega_{\text{th}} \quad \text{(loading / minor impact)}, \\ I_{\max}, & |\dot{\theta}| > \omega_{\text{th}} \quad \text{(major impact)}, \end{cases} \quad (3)$$

The current levels were set to $(I_{\text{base}}, I_{\text{low}}, I_{\max}) = (0.5, 1.0, 1.5)$ A. I_{cmd} denotes the commanded MR coil current, and $\Gamma(s) \in \{0, 1\}$ is a state-gating function determined by the FSM, where $\Gamma = 0$ during nominal locomotion and $\Gamma = 1$ in MR-enhanced states (e.g., impact mitigation and stationary support). a_z represents the vertical base acceleration measured by the onboard IMU, with a_{th} denoting a disturbance detection threshold. The joint angular velocity is denoted by $\dot{\theta}$, and ω_{th} is a velocity threshold to distinguish rapid impact motion from slow or quasi-static behavior.

C. Hardware

This section introduces the main electronic and mechanical components of the system (Fig. 3). MR_Go joints are denoted as hip (ID0), thigh (ID1), and calf (ID2) across the four limbs: Front Right (FR), Front Left (FL), Rear Right (RR), and Rear Left (RL). A four-channel MR controller, built on an STM32 microcontroller, independently regulates the MRAs on each leg through precise closed-loop PI current control for each channel. The MR controller relied on the state estimator to provide precise MR control in stabilizing the state of MR_Go. MR_Go is equipped with a LiDAR for navigation, and a human interface enables teleoperation via the stereo depth camera and remote controller. For example, the MR_Go can achieve a specimen collection task through teleoperation using a manipulator containing a bionic mechanical palm (uHand 2.0) with a 6-DoF robotic arm (Unitree K1), forming a 7-DoF system. The manipulator is operated through an exoskeleton-based teleoperation interface that mirrors the operator's hand motions and provides

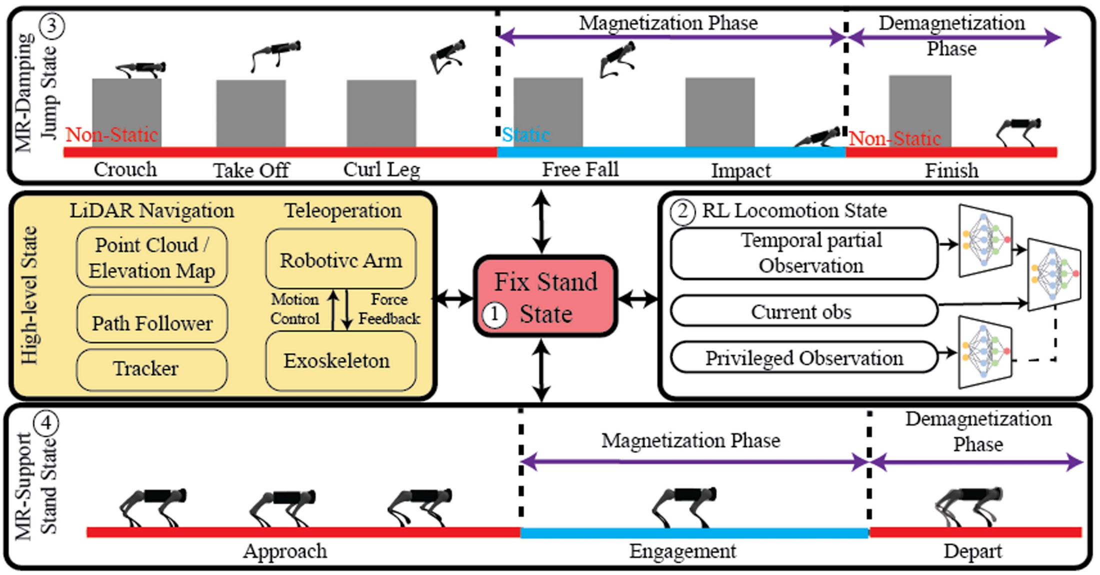

Fig. 4. Hybrid FSM architecture integrating low-level MR–electric actuation control with high-level navigation and teleoperation. The MR-Damping Jump state activates MR damping for impact mitigation during landing, while the MR-Support Stand state employs MR locking for efficient static load support. The high-level states (LiDAR Navigation and Teleoperation) operate concurrently to enable autonomous mobility and manipulation tasks.

force feedback [29]. All devices are powered and synchronized through the onboard BMS and communication buses. The MR controller communicates with the Nvidia NX via serial connection under the ROS framework, enabling real-time coordination between electric torque control and MR current regulation.

D. Hybrid FSM

The software architecture of MR_Go is built upon the Unitree Guide framework, with a custom FSM framework that integrates MR actuation into conventional electric actuation. As shown in Fig. 4, the Hybrid FSM consists of four states: ① the Fix Stand state, ② the Locomotion state, ③ the MR-Damping Jump state, and ④ the MR-Support Stand state.

The control system can switch between two purely electric states (Fix Stand and Locomotion) and two MR-enhanced states (MR-Damping Jump and MR-Support Stand). The MR-Damping Jump state and MR-Support Stand state are specifically designed to showcase the capabilities of the proposed MRA when integrated with conventional electric actuation in a quadruped robot.

The MR-Damping Jump state follows a conventional jumping sequence, divided into two phases: the Non-static Phase (takeoff) and the Static Phase (free-fall). During the Static Phase, the MRAs are activated alongside the electric actuators to dissipate impact energy upon landing, effectively reducing transmitted torque, minimizing impact-induced oscillations, and improving post-landing stability. The MR-Support Stand state works with the locomotion framework to perform an approach–engage–depart maneuver. In this state, the robot approaches a target, enters a stationary engagement phase (e.g., specimen collection or inspection), and then departs to resume locomotion. During engagement, the electric actuators' position gains are gradually reduced to zero, while the MRAs are activated in Damping Mode to provide high-torque support with minimal power consumption, demonstrating the ability to sustain loads and maintain posture stability without continuous electrical input.

In addition to these MR-enhanced states, the high-level states facilitate autonomous navigation and teleoperation. The Navigation state utilizes LiDAR-based localization and path tracking, integrating with the locomotion state for precise movement. The Teleoperation state allows manual control of the robotic arm for specimen collection, supported by the MR-Support Stand state, which enables the MRAs to handle the manipulator load efficiently without the risk of overheating or excessive power consumption.

For the Navigation state, an offline mapping method using a pre-scanned terrain map and the Normal Distributions Transform (NDT) algorithm performs Simultaneous Localization and Mapping (SLAM). To improve map precision, multiple one-dimensional static Kalman filters are applied for layered optimization, reducing noise and refining the elevation map. Path planning is achieved using an enhanced Rapidly-Exploring Random Tree (RRT) algorithm, which evaluates terrain quality with a terrain-based cost function. The path is smoothed through a quadratic programming formulation solved by the OSQP solver, generating an optimized trajectory. The Tracker state employs our RL-based locomotion pipeline, trained to navigate complex terrain and follow the planned path accurately.

Finally, the Fix-Stand state uses conventional position control to ensure stability during stationary tasks. This integrated control architecture enables MR_Go to autonomously perform dynamic locomotion, manipulate payloads, and execute impact-resilient landings during complex missions.

III. Performance Validation

A. Drop-Test Validation

The performance of MRAs integrated into MR_Go was evaluated through controlled drop tests from an initial height of 30 cm (measured from the robot's feet to the ground). In MR Damping Mode, the excitation coils were activated upon release and remained energized throughout the landing phase until

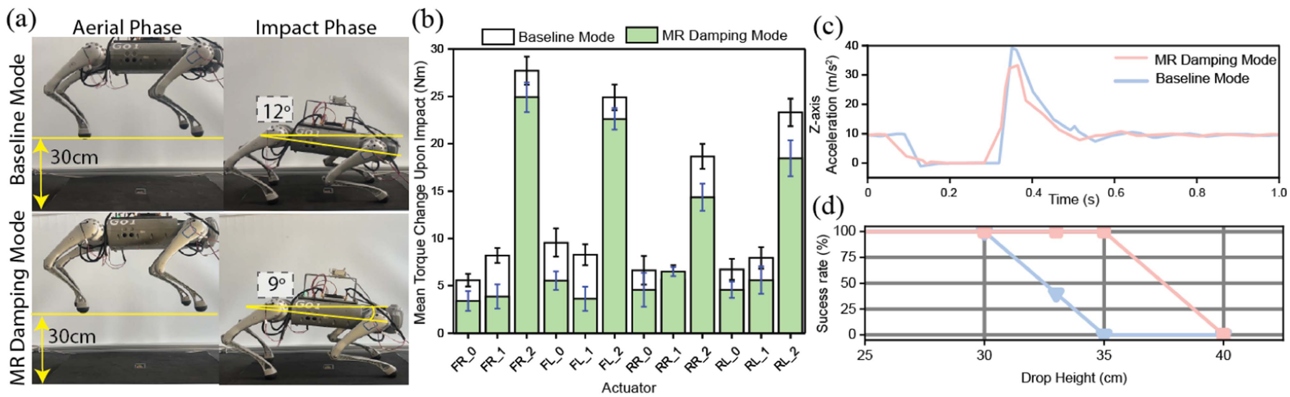

Fig. 5. Comparison between Baseline Mode and MR Damping Mode during drop-test validation. (a) Landing posture at a 30 cm drop height. (b) Mean joint torque change during impact across all 12 actuators. (c) Vertical base acceleration at impact. (d) Landing success rates over different drop heights, evaluated over 10 trials per condition.

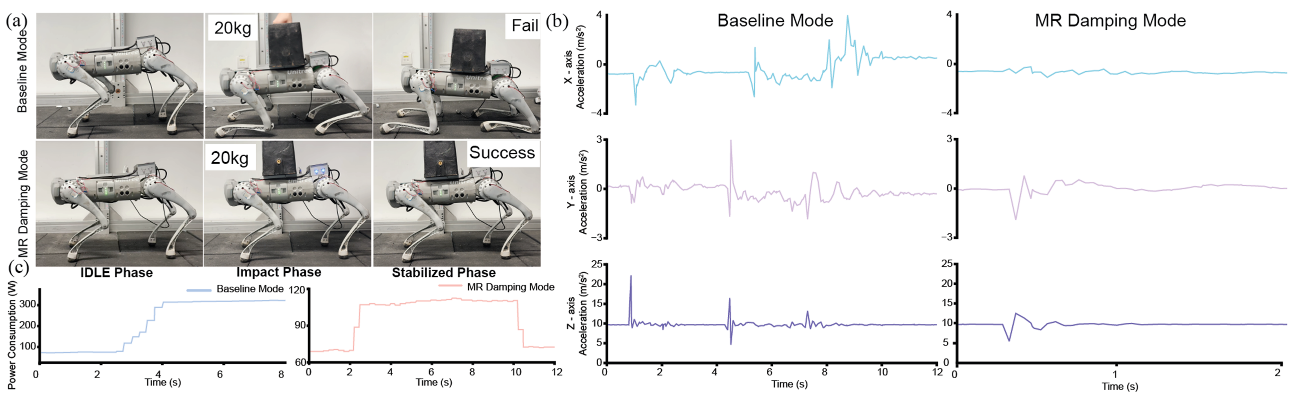

Fig. 6. Payload test. (a) Load test comparison between Baseline Mode and MR Damping Mode, with a 20kg payload. (b) XYZ acceleration profiles for both Modes, comparing the quadruped robot's stability across IDLE, Impact, and Stabilized phases. (c) Power consumption of the quadruped robot in Baseline Mode, and combined power consumption of the robot and MR controller in MR Damping Mode.

stabilization Fig. 5(a), while the baseline mode was conducted by pure electric joints. To highlight the effect of MR damping, a low actuator gain was applied in all trials, allowing assessment of MRA performance under reduced controller stiffness.

Post-landing analysis revealed a smaller body inclination compared to Baseline Mode, indicating improved impact stability. Quantitative evaluation was based on peak-to-peak torque differentials, defined as the difference between the maximum and minimum torque during impact, normalized across trials and joints. As shown in Fig. 5(b), MR Damping Mode (green bars) consistently reduced joint torque relative to Baseline Mode (open bars), with 11 of 12 actuators exhibiting reductions. The error bars denote standard deviations over 10 repeated trials. Averaged across all actuators, MR Damping Mode achieved a 23% decrease in cumulative torque, confirming its capacity for adaptive impact attenuation. Supporting this, Z-axis acceleration data Fig. 5(c) show that MR Damping Mode reduced the peak impact acceleration from 39.1 m/s^2 to 33.3 m/s^2, corresponding to a 15% reduction and faster post-landing stabilization.During impact, the elevated yield torque together with post-yield viscous damping dissipates impact energy and constrains excessive joint motion, thereby explaining the observed reduction in peak base acceleration. Landing reliability was further assessed over varying drop heights (n=10 per height). As shown in Fig. 5(d), MR Damping Mode maintained a 100% success rate at 35 cm, whereas Baseline Mode remained reliable only up to 30 cm. The reduced peak torque under MR damping enabled MR_Go to withstand higher impacts without mechanical failure or over-current trips. These results highlight the robustness and reliability of MR Damping Mode for high-impact operations in constrained or hazardous environments.

B. Payload Validation

An experimental setup was developed to evaluate the payload-handling capability of MR_Go under both MR Damping and Baseline Mode. The robot was positioned on a static surface, and a 20 kg payload was applied. In MR Damping Mode, the MRAs were activated immediately upon loading. As shown in Fig. 6(a), the process comprised three phases: IDLE (no load), Impact (initial loading), and Stabilized (postural recovery).

In Baseline Mode, the step load compressed the leg stroke, causing instability and ground contact upon release. As depicted in Fig. 6(b), this instability led to pronounced fluctuations in the X-, Y-, and Z-axis accelerations during impact, whereas MR Damping Mode maintained a stable and controlled response. The greater angular deviation in Baseline Mode caused a surge in power usage to a peak of approximately 310W.

In contrast, MR Damping Mode establishes a yield torque impedance that suppresses joint motion during load application, attenuates load-induced disturbances, and stabilizes the posture without inducing large joint displacements.

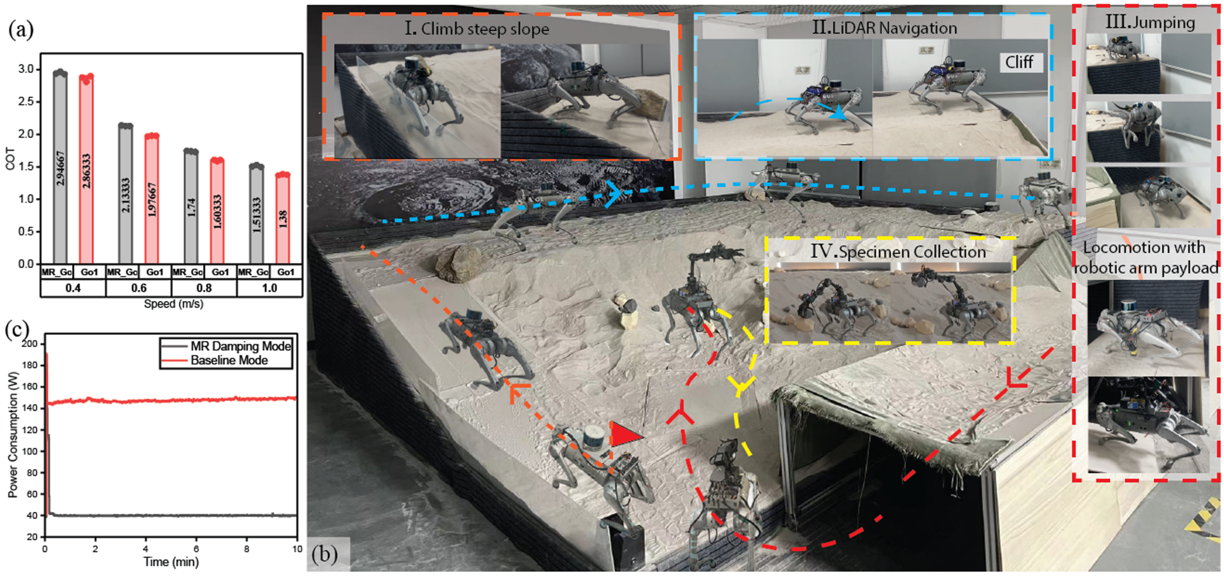

Fig. 7. Lunar-analog exploration mission and system-level performance evaluation. (a) Mean COT between the conventional Go1 and MR_Go. (b) Mission overview showing the four main task phases: (I) climbing a sandy slope, (II) LiDAR-based navigation, (III) cliff descent for robotic arm deployment, and (IV) specimen collection with a 3 kg manipulator. (c) Standardized stationary power consumption comparison without manipulator,with the robot holding an identical posture for 10 minutes under both modes.

After the excitation current was removed, the residual magnetic flux retained in the MRF continued to generate a small holding torque, enabling the robot to maintain posture under the 20 kg payload without continuous energization. To restore free joint motion for subsequent locomotion, a brief demagnetization cycle was applied to eliminate the remaining flux.

During the MR damping mode, the system consumed 70 W at IDLE, rising to 112 W during impact, approximately 40 W of which was attributed to MRA activation and stabilized at 72 W after the 8-second activation period Fig. 6(c). These results confirm that MR_Go can sustain a 20 kg payload with only a marginal 2 W increase in steady-state power, demonstrating high energy efficiency by utilizing the residual magnetic effect of the MRF to maintain support torque without continuous electrical input.

C. Impact of MR Integration on Normal Locomotion

During normal locomotion, MR actuation is disabled ($I = 0$); thus, the impact of MR integration is limited to the added distal mass of the MRA and a passive off-state drag torque τ_{off}. Fig. 7(a) compares the COT of the conventional Go1 and MR_Go across a range of forward speeds, indicating a modest increase in COT for MR_Go.

The COT increase ranges from 2.9% at low speed to 9.4% at 1.0 m/s. The small difference at 0.4 m/s indicates that τ_{off} remains limited during normal walking. At higher speeds, the larger COT gap is mainly attributed to the added distal mass, together with secondary drivetrain effects such as additional mechanical interfaces and assembly tolerances, which lead to increased friction and vibration at higher joint velocities. Importantly, this increase remains modest and does not indicate abnormal joint behavior or locomotion instability when MR actuation is inactive.

Within the targeted mission profile, continuous locomotion represents only part of the operational timeline, while the primary benefits of MR actuation arise during stationary load support and impact mitigation, where significant energy savings and improved thermal performance are demonstrated.

D. Lunar-Analog Exploration Mission

To evaluate the robustness of the MRAs under prolonged operation, a lunar-analog exploration mission was conducted using MR_Go in both MR Damping and Baseline Modes. The test area spanned 30 m^2 and was composed of fine sediment and scattered boulders resembling lunar south-pole terrain, with a total traversal distance of approximately 25 m. The mission objective was to navigate MR_Go to a simulated lunar station for manipulator installation and specimen collection. As shown in Fig. 7(b), MR_Go climbed a 20° slope, performed LiDAR-based localization and mapping, executed an 80 cm cliff descent, installed a 3 kg robotic arm, and collected a rock sample before returning to base. The robot completed all tasks without hardware failures or battery replacement. Both modes successfully achieved full mission completion within 25 minutes. Mission performance was evaluated through BMS State-of-Charge (SoC) data (Table II). During navigation and manipulator installation, MR_Go operated without MR actuation; SoC variations in these phases stemmed from terrain irregularities such as soft sand. The most significant difference appeared during specimen collection, where MR Damping Mode consumed 15% less SoC than the Baseline Mode. In addition, Fig. 7(c) provides a standardized 10-minute stationary comparison (no external payload, identical posture), showing that MR Damping Mode maintains a low steady-state power of ∼40 W versus ∼145 W in Baseline Mode, supporting the reduced motor thermal loading observed in the following mission data. By the end of the exploration, SoC dropped by 68% in Baseline Mode and 50% in MR Damping Mode, marking an 18% improvement in overall energy efficiency.

Energy conservation was primarily achieved during the 10-minute specimen collection phase using the MR-Locking Stand

TABLE I
COMPARATIVE ANALYSIS QUADRUPED ROBOTS WITH DIFFERENT ACTUATION MECHANISMS

Robot	Year of Introduction	Actuation	Static Power Consumption (W)	Mass (kg)	Static Payload (kg)	Static Payload-mass Fraction
StarIETH [8]	2013	SEA	N/A	23	25	1.08
ANYmal [7]	2016	SEA	100	30	10	0.33
MIT Cheetah III [14]	2018	QDD	N/A	45	20	0.44
Spot [15]	2019	QDD	N/A	32.7	14	0.45
Tachyon [12]	2021	SPEA	60[1]	41	20	0.49
Go1 [16]	2021	QDD	150	12	5	0.41
A - MR_Go (Ours)	2025	MRA	40	12	20	1.67

Notes: N/A = No data available. 1: Excluding computational power consumption.
Static power consumption is measured under *no external load* and *no locomotion* (IDLE condition).
Static payload denotes the maximum *quasi-static load-support capability* without locomotion, where joints maintain posture under load.

TABLE II
PLANETARY EXPLORATION'S TIMESCALE AND ASSOCIATED SOC CHANGE

Controller	Quantity	Incline	Alignment	Navigation	Alignment	Jumping	Ingress Lunar Station	Robotic Manipulator Installation	Egress Lunar Station	Specimen Collection Task	Return Lunar Station	Total
Baseline Mode	Elapsed time (min)	0.3	1.67	1.41	2.06	0.31	0.24	3	3.86	10.5	1.07	24.4
	SoC Drop (%)	5	3	7	0	2	2	3	18	26	2	68
MR Damping Mode	Elapsed time (min)	0.25	1.64	1.46	1.39	0.17	0.17	3.05	1.07	10.01	1.24	20.4
	SoC Drop (%)	2	2	7	1	1	1	4	19	11	2	50

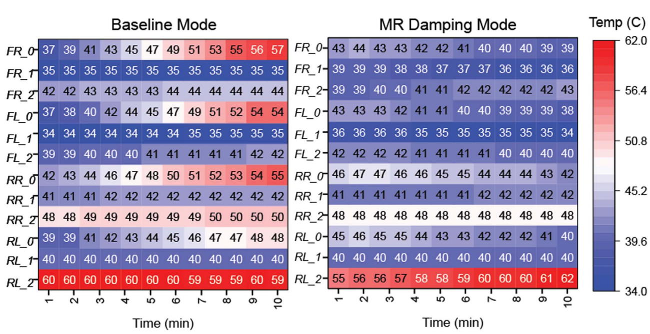

Fig. 8. Thermal profiles of all actuators during specimen collection, showing temperature reduction achieved by MR Damping Mode.

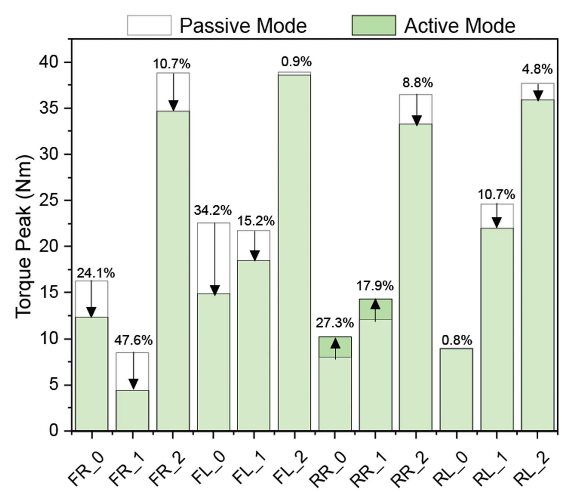

Fig. 9. Torque peak comparison between Baseline and MR Damping Modes during an 80cm cliff descent.

FSM, during which MR_Go supported a 3 kg manipulator payload with a 56% lower SoC drop compared to Baseline Mode. Actuator temperature was measured using the embedded temperature sensor located on the motor driver PCB and is visualized in the heat maps in Fig. 8. In Baseline Mode, the average actuator temperature increased from 41.1 °C to 46.8 °C, whereas under MR Damping Mode it decreased from 43.0 °C to 42.0 °C.One actuator (RL_2) exhibits a non-monotonic temperature trend in Baseline Mode, which is attributed to task-dependent asymmetry in posture and load distribution on the sandy terrain, leading to variations in current demand and non-uniform heat distribution in the driver electronics. Importantly, the overall thermal trend remains consistent even when excluding RL_2 from the average. These results indicate improved thermal stability during stationary load support, thereby reducing the risk of overheating-induced shutdowns.

Impact mitigation was evaluated during the 80 cm cliff descent. The MR-Damping Jump FSM employed high actuator gains to test MR damping under stiff control conditions. As shown in Fig. 9, torque peaks decreased in ten of twelve actuators, with minor increases in two due to landing asymmetries. Averaged across all joints, MR Damping Mode reduced peak torque by approximately 10%, validating its effectiveness in suppressing impact shocks during planetary descent.

IV. CONCLUSION

This letter demonstrates that replacing the conventional actuator with MR-based robotic joint (MR-Joint) can improve energy efficiency, payload capability, and impact mitigation. The MR-based quadruped robot demonstrated high operational efficiency and reliability during prolonged mission tasks with

MR-Joint. The current locomotion framework does not implement real-time coordination between MR actuation and electric motor actuation during gait cycles. This is primarily due to the complexity of unstructured terrains, which demand an external decision-making controller to assess terrain conditions and gait phases before activating the MRA. As a result, MRA activation was limited to discrete task phases (e.g., landing or load application). While this approach ensures the validity of the reported results, it restricts the full potential of MR actuation during continuous, terrain-adaptive locomotion. Future research should aim to integrate MR actuation into dynamic locomotion phases by developing synchronization strategies that align MR actuation engagement with stance and impact events. Such coordination would enable efficient torque sharing between MR damping and electric motor control, improving energy efficiency, load distribution, and impact mitigation. In addition, extended thermal characterization of MR actuation under sustained high-frequency dynamic excitation is identified as future work to further assess long-term thermal robustness. These advancements will be essential for achieving robust and energy-efficient locomotion in unstructured or extraplanetary environments, ultimately broadening the operational capability of legged robotic systems.

References

[1] C. Li and K. Lewis, "The need for and feasibility of alternative ground robots to traverse sandy and rocky extraterrestrial terrain," *Adv. Intell. Syst.*, vol. 5, no. 3, 2023, Art. no. 2100195.

[2] H. Kolvenbach, C. Bärtschi, L. Wellhausen, R. Grandia, and M. Hutter, "Haptic inspection of planetary soils with legged robots," *IEEE Robot. Automat. Lett.*, vol. 4, no. 2, pp. 1626–1632, Apr. 2019.

[3] O. Bilgin and F. A. Kazan, "The effect of magnet temperature on speed, current and torque in PMSMs," in *Proc. 22th Int. Conf. Elect. Machines*, 2016, pp. 2080–2085.

[4] C. Semini, N. G. Tsagarakis, E. Guglielmino, M. Focchi, F. Cannella, and D. G. Caldwell, "Design of HYQ–A hydraulically and electrically actuated quadruped robot," *Proc. Inst. Mech. Engineers, Part I: J. Syst. Control Eng.*, vol. 225, no. 6, pp. 831–849, 2011.

[5] G. Zancewicz and C. Hoefken, "Impact of actuator torque density on expected robot life-a dynamic model," in *Proc. 5th Int. Conf. Control Robot. Eng.*, 2020, pp. 30–36.

[6] M. Hutter, C. D. Remy, M. A. Hoepflinger, and R. Siegwart, "High compliant series elastic actuation for the robotic leg ScarlETH," in *Field Robotics*. Singapore: World Scientific, 2012, pp. 507–514.

[7] M. Hutter et al., "ANYmal-a highly mobile and dynamic quadrupedal robot," in *Proc. IEEE/RSJ Int. Conf. Intell. Robots Syst.*, 2016, pp. 38–44.

[8] M. Hutter, "Starleth & co.: Design and control of legged robots with compliant actuation," Ph.D. dissertation, ETH Zurich, Zürich, Switzerland, 2013.

[9] F. Guenther, H. Q. Vu, and F. Iida, "Improving legged robot hopping by using coupling-based series elastic actuation," *IEEE/ASME Trans. Mechatronics*, vol. 24, no. 2, pp. 413–423, Apr. 2019.

[10] S. Liu, J. Ding, C. Lu, Z. Wang, B. Su, and Z. Guo, "A novel optimization design of dual-slide parallel elastic actuator for legged robots," *IEEE/ASME Trans. Mechatronics*, vol. 29, no. 4, pp. 2886–2894, Aug. 2024.

[11] F. Bjelonic et al., "Learning-based design and control for quadrupedal robots with parallel-elastic actuators," *IEEE Robot. Automat. Lett.*, vol. 8, no. 3, pp. 1611–1618, Mar. 2023.

[12] Y. Kamikawa et al., "Tachyon: Design and control of high payload, robust, and dynamic quadruped robot with series-parallel elastic actuators," in *Proc. 2021 IEEE/RSJ Int. Conf. Intell. Robots Syst.*, 2021, pp. 894–901.

[13] E. Koco, A. Mutka, and Z. Kovacic, "New variable passive-compliant element design for quadruped adaptation to stiffness-varying terrain," *Int. J. Adv. Robotic Syst.*, vol. 13, no. 3, 2016, Art. no. 90.

[14] G. Bledt, M. J. Powell, B. Katz, J. D. Carlo, P. M. Wensing, and S. Kim, "MIT cheetah 3: Design and control of a robust, dynamic quadruped robot," in *Proc. IEEE/RSJ Int. Conf. Intell. Robots Syst.*, 2018, pp. 2245–2252.

[15] B. Dynamics, "Spot," 2021. Accessed: Apr. 21, 2025. [Online]. Available: https://bostondynamics.com/products/spot/

[16] Unitree Robotics, "Go1," 2016. Accessed: Apr. 21, 2025. [Online]. Available: https://www.unitree.com/cn/go1

[17] J. D. Vicente, D. J. Klingenberg, and R. Hidalgo-Alvarez, "Magnetorheological fluids: A review," *Soft Matter*, vol. 7, no. 8, pp. 3701–3710, 2011.

[18] M. Christie, S. Sun, L. Deng, H. Du, S. Zhang, and W. Li, "Real-time adaptive leg-stiffness for roll compensation via magnetorheological control in a legged robot," *Smart Mater. Structures*, vol. 31, no. 4, 2022, Art. no. 045003.

[19] S. Huang, B. Chen, M. Yin, Y. Ren, and Z. Xie, "Optimal design of shock absorption for hexapod robot based on magnetorheological fluid," *J. Phys. Conf. Ser.*, vol. 2361, no. 1. 2022, Art. no. 012025.

[20] J.-S. Plante, A. St-Jean, and J.-P. Lucking Bigué, "Bridging the gap between haptic devices and cobots with highly geared magnetorheological actuators," *Sci. Rep.*, vol. 15, no. 1, 2025, Art. no. 14363.

[21] C. Véronneau et al., "Multifunctional remotely actuated 3-DoF supernumerary robotic arm based on magnetorheological clutches and hydrostatic transmission lines," *IEEE Robot. Automat. Lett.*, vol. 5, no. 2, pp. 2546–2553, Apr. 2020.

[22] X. Mai et al., "Non-motorized hand exoskeleton for rescue and beyond: Substantially elevating grip endurance and strength," *IEEE Trans. Robot.*, vol. 41, pp. 4761–4775, 2025.

[23] J. Song, A. Zhu, Y. Tu, C. Zheng, and G. Cao, "Magnetorheological damper with variable displacement permanent magnet for assisting the transfer of load in lower limb exoskeleton," *IEEE Trans. Neural Syst. Rehabil. Eng.*, vol. 32, pp. 43–52, 2023.

[24] E. Kostamo et al., "Magnetorheologically damped compliant foot for legged robotic application," *J. Mech. Des.*, vol. 136, no. 2, 2014, Art. no. 021003.

[25] Y. Erwin, L. Wenbo, M. Xianlong, C. Zirui, Z. Liang, and S. Shuaishuai, "Development of a magnetorheological-based electrical robotic joint with characteristics of high load capability and high energy efficiency," *Smart Mater. Structures*, in press.

[26] A. Ghaffari, S. H. Hashemabadi, and M. Ashtiani, "A review on the simulation and modeling of magnetorheological fluids," *J. Intell. Mater. Syst. Structures*, vol. 26, no. 8, pp. 881–904, 2015.

[27] M. Zubieta, S. Eceolaza, M. Elejabarrieta, and M. Bou-Ali, "Magnetorheological fluids: Characterization and modeling of magnetization," *Smart Mater. Structures*, vol. 18, no. 9, 2009, Art. no. 095019.

[28] H. Ma, B. Chen, L. Qin, and W.-H. Liao, "Design and testing of a regenerative magnetorheological actuator for assistive knee braces," *Smart Mater. Structures*, vol. 26, no. 3, 2017, Art. no. 035013.

[29] Z. Kong et al., "A force feedback exoskeleton for teleoperation using magnetorheological clutches," 2025, *arXiv:2506.15124*.